Cells & Development xxx (xxxx) xxx

Contents lists available at ScienceDirect

Cells & Development

journal homepage: www.journals.elsevier.com/cells-and-development

Nonlinear rheology of cellular networks

Charlie Duclut [a,1], Joris Paijmans [a,1], Mandar M. Inamdar [b], Carl D. Modes [c,d,e], Frank Jülicher [a,d,e,*]

[a] Max Planck Institute for the Physics of Complex Systems, Nöthnitzer Str. 8, 01187 Dresden, Germany
[b] Department of Civil Engineering, Indian Institute of Technology Bombay, Powai, Mumbai 400076, India
[c] Max Planck Institute for Molecular Cell Biology and Genetics (MPI-CBG), Dresden 01307, Germany
[d] Center for Systems Biology Dresden, Pfotenhauerstrasse 108, 01307 Dresden, Germany
[e] Cluster of Excellence, Physics of Life, TU Dresden, Dresden 01307, Germany

ARTICLE INFO

Keywords:
Tissue mechanics
Cell mechanics
Nonlinear rheology
Vertex model
Continuum theory

ABSTRACT

Morphogenesis depends crucially on the complex rheological properties of cell tissues and on their ability to maintain mechanical integrity while rearranging at long times. In this paper, we study the rheology of polygonal cellular networks described by a vertex model in the presence of fluctuations. We use a triangulation method to decompose shear into cell shape changes and cell rearrangements. Considering the steady-state stress under constant shear, we observe nonlinear shear-thinning behavior at all magnitudes of the fluctuations, and an even stronger nonlinear regime at lower values of the fluctuations. We successfully capture this nonlinear rheology by a mean-field model that describes the tissue in terms of cell elongation and cell rearrangements. We furthermore introduce anisotropic active stresses in the vertex model and analyze their effect on rheology. We include this anisotropy in the mean-field model and show that it recapitulates the behavior observed in the simulations. Our work clarifies how tissue rheology is related to stochastic cell rearrangements and provides a simple biophysical model to describe biological tissues. Further, it highlights the importance of nonlinearities when discussing tissue mechanics.

1. Introduction

During morphogenesis, cells divide, die, rearrange, and flow to create complex structures and shape organs. On short time scales, cells maintain tissue mechanical integrity and form a solid-like structure, while at longer time scales, tissues can deform and relax internal stresses, thus behaving as viscous fluids. In order to understand morphogenetic processes, the physical and mechanical properties of tissues as an active complex material are important. In material sciences, the study of time-dependent deformations and flows of a material under shear is called rheology.

The rheology of confluent tissues plays a role in many key physiological processes such as cell migration, wound healing, cancer metastasis, and morphogenesis and dictates the deformation response of the tissue with respect to both external and internal forcing (Petridou and Heisenberg, 2019; Barriga and Mayor, 2019). At one end of the spectrum, tissues can behave as elastic solids in which they deform under the application of force and retract back to their original shape upon removal of the load. At the other end of the spectrum, tissues can exhibit fluid-like behavior in which they deform under forcing and retain that deformation upon the removal of the forcing (Barriga and Mayor, 2019). Tissues can also display viscoelastic material properties. Viscoelastic liquids typically exhibit short-time elastic and long-time viscous behavior, while viscoelastic solids are short-time viscous and long-time solid (Forgacs et al., 1998). Tissues can also show plastic material properties such that they behave as elastic solids but, for stresses that exceed the yield stress, start to flow and behave more fluid-like (Molnar and Labouesse, 2021).

Tissue rheology and, in particular, tissue fluidization in confluent tissues involve topological rearrangements of the cellular network such as cell divisions, cell extrusions, and cell neighbor exchanges (T1 transitions) (Guirao et al., 2015; Etournay et al., 2015). One common mode of tissue fluidization is by topological transitions that bring about cell rearrangements. This mode is important for example during avian and zebrafish gastrulation (Firmino et al., 2016; Saadaoui et al., 2020; Petridou et al., 2019). In addition, cell division and growth can also lead to

* Corresponding author.
E-mail address: julicher@pks.mpg.de (F. Jülicher).
[1] These authors contributed equally.

https://doi.org/10.1016/j.cdev.2021.203746
Received 30 March 2021; Received in revised form 19 June 2021; Accepted 13 September 2021
Available online 27 September 2021

fluidization of tissues (Ranft et al., 2010). Cell division can involve cell rearrangements, for example due to a combination of cell rounding during mitosis and cellular rearrangement afterwards (Firmino et al., 2016; Petridou et al., 2019). However, it has also been suggested that cellular crowding due to cell proliferation can lead to a solid-like state of the tissue, especially in the presence of strong cell-cell adhesions (Angelini et al., 2011; Garcia et al., 2015). Tissue deformations can result from active processes, for example by actively-generated cell shape changes or due to contraction of the acto-myosin network (Molnar and Labouesse, 2021; Vuong-Brender et al., 2017; Bailles et al., 2019).

The global rheological properties of tissues are dependent on cell-level characteristics such as shape, size, contractility, and motility (Mitchel et al., 2020). A combination of cadherin-mediated adhesion and acto-myosin contractility controls the dynamics of cell-cell junctions (Mongera et al., 2018; Curran et al., 2017). There is evidence that increase in cell-cell adhesion can lead to tissue fluidization in confluent tissues, and that cell geometry is a good indicator of tissue unjamming (Bi et al., 2015; Atia et al., 2018). Moreover, combining mechanical perturbation by laser ablations with the quantification of cell elongation changes permits to investigate epithelial viscoelasticity (Iyer et al., 2019). Importantly, tissues mechanical properties are not constant in time but can be actively modulated by chemical patterns and genetic programs (Petridou et al., 2019; Heisenberg and Bellaïche, 2013; Duda et al., 2019). There is increasing evidence that morphogenetic signals, such as Wnt/PCP, can control tissue mechanical properties by governing the cell level properties such as contractility, division and cell-cell adhesion (Barriga and Mayor, 2019; Petridou et al., 2019; Bosveld et al., 2012; Arraf et al., 2020).

Heterogeneity and fluctuations at the cell level also play a significant role in tissue fluidization by facilitating the relaxation of local stresses (Curran et al., 2017; Beysens et al., 2000; Marmottant et al., 2009; Tetley et al., 2019). Tension fluctuations, which have for instance been studied in detail in *Drosophila* (Curran et al., 2017) and in zebrafish embryos (Mongera et al., 2018; Kim et al., 2020), are especially relevant as they can trigger T1 transitions and therefore lead to tissue flows. The importance of fluctuations for tissue fluidization has also been investigated numerically both with vertex model simulations (Curran et al., 2017; Kim et al., 2020; Bi et al., 2016; Krajnc et al., 2018; Sussman et al., 2018; Yamamoto et al., 2020) and cellular Potts model simulations (Marmottant et al., 2009; Chiang and Marenduzzo, 2016). These fluctuations, introduced as a noise in the vertex positions (Sussman et al., 2018) or in the form of bond tension fluctuations (Curran et al., 2017; Kim et al., 2020; Krajnc et al., 2018; Yamamoto et al., 2020), lead in both cases to a glassy transition when the magnitude of the noise is varied.

Great effort has been put into the characterization of these glassy dynamics in terms of state diagrams, and their signature on cell motion has been studied extensively, for instance in terms of mean-square displacement of the particles or effective diffusivity (Kim et al., 2020; Bi et al., 2016; Chiang and Marenduzzo, 2016). However, the role of tension fluctuations and active noises on the macroscopic rheological properties of cell networks remains poorly characterized, and a nonlinear coarse-grained description of these systems that would capture the glassy transition is still missing. Coarse-grained descriptions of tissues, using for instance tools from active gels and active hydrodynamics (Marchetti et al., 2013; Prost et al., 2015), have proven extremely valuable to characterize tissue fluidization by death and growth (Ranft et al., 2010) or to exhibit the role of electric and hydraulic phenomena in tissues (Sarkar et al., 2019; Duclut et al., 2019; Duclut et al., 2021). These models can then in turn provide new insights to understand morphogenetic events, for instance the role of mechosensitive feedback in the *Drosophila* wing imaginal disc development (Dye et al., 2020).

In this theoretical paper, we perform a systematic study of the role of bond tension fluctuations on the rheological properties of cellular networks. Our analysis is guided by a two-dimensional vertex model, which has been shown to provide a remarkable agreement with experimental data in the case of *Drosophila* wing morphogenesis (Etournay et al., 2015) and for other confluent monolayers (Tetley et al., 2019; Alt et al., 2017; Fletcher et al., 2014; Comelles et al., 2021). To quantify the dynamical deformations of the cell network and relate them to cellular processes, we use a shear decomposition based on a triangulation of the cell network (Merkel et al., 2017). This analysis reveals how large scale tissue shape changes are dominated at short time by cell elongation and at long time by cell rearrangements. We use different triangulations and show that some measures are robust and independent of the triangulation used, while others depend on the choice of triangulation.

Using this approach, we study the relationship between stress and strain rate in tissues. We observe nonlinearities in the stress versus strain rate relationship of the vertex model for all magnitudes of the fluctuations. Finally, we show that a generic nonlinear description of the material properties of cell networks can account for them.

The paper is organized as follows. In Section 2, we introduce the vertex model and its work function. Using two different triangulation methods, we then analyze the dynamics of the system under pure shear in Section 3. We show that the dynamics has nonlinear effects that cannot be captured by a linear continuum description. We then introduce and discuss a nonlinear model in Section 4, both in the case of an isotropic cell network and in the case of a network with an intrinsic anisotropy.

2. Mechanics of polygonal cell networks

The cell boundaries, defined as the network of apical cellular junctions of epithelial tissues, form a 2D network that is well-represented by a packing of convex polygons. The mechanics of this network can be described by a vertex model, where cells are represented as polygons that are outlined by straight edges connecting vertices (Farhadifar et al., 2007). In this section, we briefly review the vertex model and describe the dynamics of the polygonal cell network arising from bond tension fluctuations, topological rearrangements in the network, and dynamic boundary conditions.

2.1. Work function of the cell network

We consider a polygonal cell network consisting of N_c polygonal cells labeled α, N_v vertices labeled m and N_b straight bonds between connected vertices labeled $\langle mn\rangle$ where m and n are the vertices they connect. Each cell is characterized in terms of its area A^α, its perimeter L^α and the lengths of the bonds that form the outline of the cell $\mathcal{L}_{mn}$, as shown in Fig. 1.

We employ a quasistatic representation of epithelia where the cell network is at any instant in a mechanical equilibrium, while the parameters describing cell properties can slowly change with time. At each vertex m, the total force $\mathbf{F}_m = -\partial W_0/\partial \mathbf{R}_m$ vanishes, where $\mathbf{R}_m$ is the position of the vertex, and W_0 is the vertex model work function and reads (Farhadifar et al., 2007; Honda et al., 1984):

$$W_0 = \sum_\alpha \frac{1}{2} K^\alpha \left(A^\alpha - A_0^\alpha\right)^2 + \sum_{\langle m,n\rangle} \Lambda_{mn}\mathcal{L}_{mn} + \sum_\alpha \frac{1}{2}\Gamma^\alpha (L^\alpha)^2. \quad (1)$$

Note that for clarity, upper-case letters are used here and in the following for quantities related to the vertex model, while lower-case letters will be used for the continuum model. The first term describes an area elasticity contribution, with A_0^α the preferred cell area and K^α the area stiffness. This term arises from the shear elasticity of cells that keep their volume roughly constant. The second term describes a contribution due to the tension of network bonds with length $\mathcal{L}_{mn}$ and line tension Λ_{mn}. This tension is usually positive, favoring the shrinking of the bonds, but could also be negative, favoring an extension of the bonds. The third term describes an elasticity of the cell perimeter with stiffness Γ^α. For simplicity, we use for all cells the same constant values of the parameters

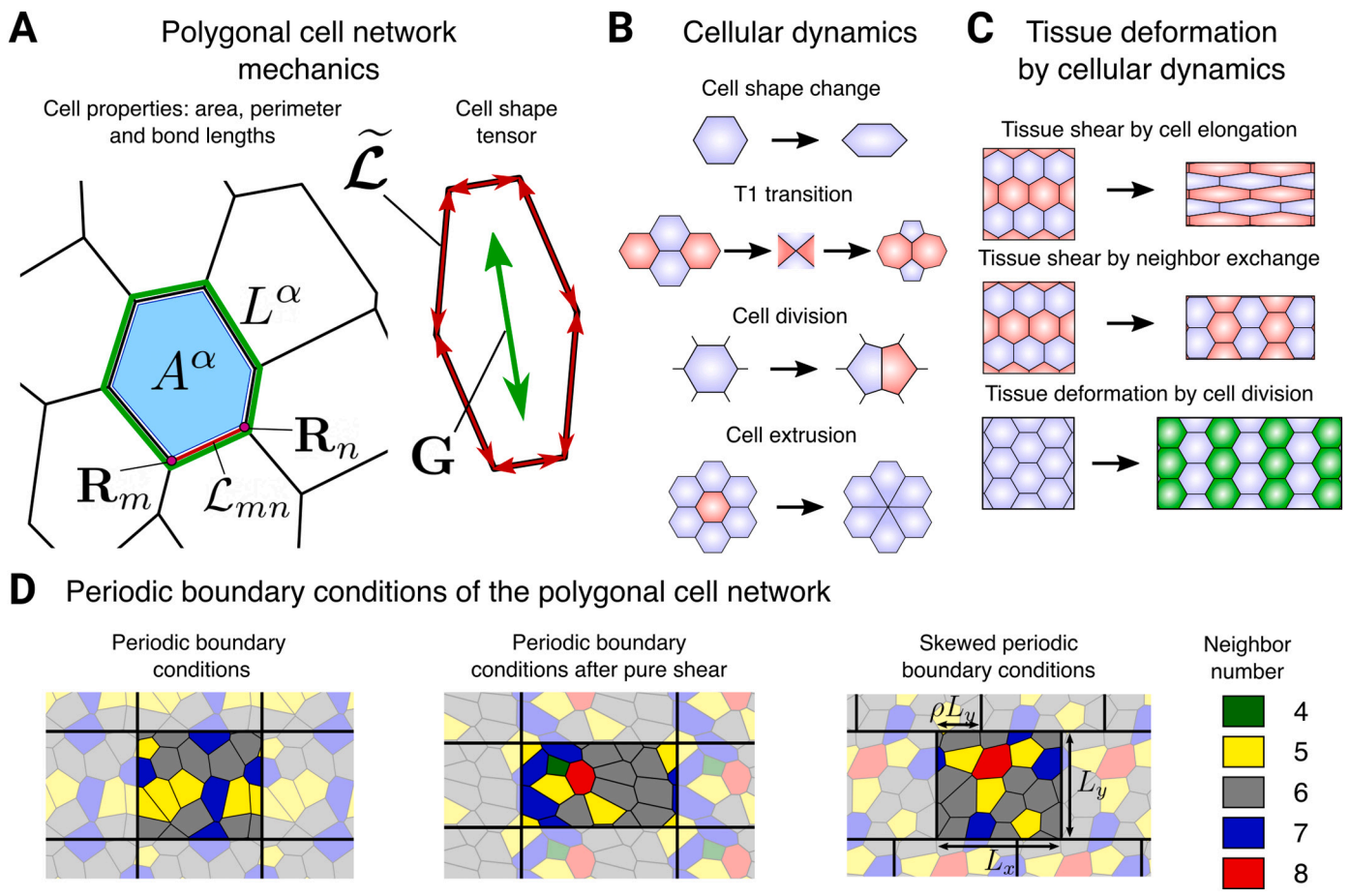

Fig. 1. Mechanics and dynamics of cellular networks. (A) Definition of the cell state variables. Left shows the cell area A^α (blue patch), cell perimeter L^α (green line) and bond length $\mathcal{L}_{mn}$ (red line) between the vertices with positions $\mathbf{R}_m$ and $\mathbf{R}_n$. Right shows the cell elongation tensor $\mathbf{G}$ which is constructed from the bond nematic tensors $\tilde{\mathcal{L}}$ as defined in Eq. (13). (B) Cell dynamic processes can lead to tissue deformation as an effect of cell shape changes, T1 transitions, cell divisions or cell extrusions. (C) Large scale tissue deformation can be driven by collective cell dynamics: cell shape changes (top), anisotropic T1 transitions (middle) and anisotropic cell divisions (bottom). The tissue may deform as a result of changes in the mean cell shape of the cellular network. Alternatively, when T1 transitions preferably occur on edges with a certain orientation, the resulting rearrangement of the cells can induce tissue shear. Cell divisions with a preferred division axis (vertical in the figure), the division and the subsequent growth of the cells can induce a tissue deformation (new cells are colored green). (D) Boundary conditions used in this paper. Cell colors indicate the neighbor number, given in the legend to the right. Adapted from Merkel, 2014.

K^α, A_0^a and Γ^α. In App. A, we give details on the numerical implementation of the vertex model. Values of the (dimensionless) parameters used in the simulations are given in Table 1 (see Supplementary material).

2.2. Bond tension fluctuations and topological network rearrangements

For a fixed connectivity of cells, the cellular network as defined above behaves purely elastically under external deformations. However, tissues are known to undergo plastic deformations and can exhibit viscoelastic behaviors (Guirao et al., 2015; Etournay et al., 2015). This is because they are able to relax internal stresses due to topological rearrangements such as cell neighbor exchanges, cell divisions and cell extrusions (Forgacs et al., 1998; Ranft et al., 2010; Marmottant et al., 2009), see Fig. 1. In the absence of external stresses, topological rearrangements and cell neighbor exchanges (or "T1 transitions") can be driven by fluctuations of the bond lengths in the cell network (Mongera et al., 2018; Curran et al., 2017; Tetley et al., 2019). In tissues, these fluctuations could be due to variations in the mechanical properties of cell bonds due to the binding and unbinding of adhesion proteins to the cell membrane or changes of the contractility in the cell cortex. We capture this dynamics by a time-dependent line tension $\Lambda_{mn}(t)$. The line tension dynamics of individual bonds in the network follows an Ornstein-Uhlenbeck process:

$$\frac{d\Lambda_{mn}}{dt} = -\frac{1}{\tau_\Lambda}(\Lambda_{mn}(t) - \Lambda_0) + \Delta\Lambda\sqrt{2/\tau_\Lambda}\,\Xi_{mn}(t), \tag{2}$$

where $\Xi_{mn}(t)$ is a Gaussian white noise with zero mean $\langle\Xi_{mn}(t)\rangle=0$, and correlations $\langle\Xi_{mn}(t)\Xi_{op}(t')\rangle = \delta_{\langle mn\rangle,\,\langle op\rangle}\delta(t-t')$ where $\delta_{\langle mn\rangle,\,\langle op\rangle}=1$ if vertices $\langle mn\rangle$ and $\langle op\rangle$ are the same and 0 otherwise (Farhadifar et al., 2007; Aigouy et al., 2010). The line tension of every bond relaxes towards its mean value Λ_0 with a characteristic time τ_Λ, which sets the time scale of the dynamics and is of the order of the acto-myosin cortex turnover time. Note that this time scale has recently been shown to play a role in the rigidification of the tissue through the formation of "trapped" edges (Yamamoto et al., 2020). Finally, the magnitude of bond tension fluctuations $\Delta\Lambda$ has a crucial role in the rheological properties of cell networks, as we discuss in Section 4.

2.3. Boundary conditions and time dependent shear deformations

In order to study the rheological properties of the stochastic vertex model, we consider a cell network in a rectangular box with dimensions L_x and L_y with periodic boundary conditions, as shown in Fig. 1, panel D.

Throughout the paper, we will apply three different boundary conditions. (i) Under a *fixed* boundary condition, the box dimensions L_x and L_y do not change over time. (ii) Under a *pure shear* boundary condition, the box dimensions are deformed as $L_x = {L_x}^0 \exp(\rho(t))$ and $L_y = {L_y}^0 \exp(-\rho(t))$, such that the aspect-ratio of the box changes but the area remains fixed. At constant shear rate V_0, one has $\dot{\rho} = V_0$, where the dot stands for the time derivative. (iii) Under a *simple shear* boundary condition, the dimension of the simulation box are kept fixed and we apply a skewed periodic boundary condition or Lees-Edwards boundary condition (Lees and Edwards, 1972): each bond in the network that crosses the horizontal boundary of the periodic box obtains an extra skew ρL_y in the horizontal direction (see Fig. 1D). Finally, we define the shear stress acting on the simulation box: $\Sigma_0 = {L_x}^{-1}{L_y}^{-1}\partial W/\partial\rho$. We provide five movies in the Supplemental material to illustrate examples of vertex model simulations under different boundary conditions. See Movie 1 for an example of simple shear, Movie 2 for an example of pure shear and Movie 5 for an example of fixed boundary condition. Descriptions of the movies are given in App. E.

3. Dynamics of a polygonal cell network under pure shear

The deformation of a cellular network is quantified by the shear rate V_0. The overall shear of the network can be decomposed into cellular contributions. For flat triangulated networks, such a decomposition can be done exactly (Etournay et al., 2015; Merkel et al., 2017). Following Etournay et al., 2015 and Merkel et al., 2017), starting from a polygonal cellular network we can use a *dual lattice* triangulation to define the shear decomposition. We assign to each three-fold vertex of a polygon a triangle[2]. The triangle corners are the area-weighted geometric centers of three polygons that meet at the vertex, see Fig. 2. This choice of triangulation of the polygonal network is however not unique.

To discuss the role of triangulation on the shear decomposition, we also use an alternative, *subcellular* triangulation. These subcellular triangles are defined by connecting the geometric center of each cell polygon to two consecutive vertices, see Fig. 2A. Subcellular triangulation has the advantage that each triangle is associated with a single cell, while in the dual lattice triangulation, each triangle is associated with three cells. Although the total tissue shear is the same for any triangulation, the specific choice of triangulation has an impact on the decomposition of shear. We analyze the vertex model dynamics using these two complementary triangulations. Because in the vertex model we have precise knowledge of the time dependence of the polygonal shapes and their connectivity, we gain a clear understanding of which quantities are independent of the triangulation and which ones are not. We present this analysis in the following.

3.1. Quantifying cellular contributions to tissue deformation

To study the dynamical response of an isotropic cellular network under shear flow, we use the stochastic vertex model introduced in Section 2 with pure shear boundary conditions and analyze its dynamics using the two different triangulations introduced above. Following Merkel et al., 2017, the large-scale shear-rate tensor $\widetilde{V}_{ij}$ of the cellular network can be decomposed as:

$$\widetilde{V}_{ij} = \frac{\mathrm{D}Q_{ij}}{\mathrm{D}t} + R_{ij}. \tag{3}$$

Here and in the following, i and j corresponds to 2d Cartesian indices, Q_{ij} is the mean cell elongation tensor and D/Dt is the corotational time derivative of a tensor (defined in Eq. (C3) of App. C). The tensor R_{ij} accounts for shear rate due to topological rearrangements and is a sum of four contributions:

$$R_{ij} = T_{ij} + C_{ij} + E_{ij} + D_{ij}, \tag{4}$$

where the tensors T_{ij}, C_{ij} and E_{ij} account for shear rate due to T1 transitions, cell divisions and cell extrusions, respectively. Note that we focus on cell networks where cell number is constant and such that, by good approximation, $C_{ij} \simeq 0$ and $E_{ij} \simeq 0$ (see App. A4 for details). The tensor D_{ij} is a shear rate associated with heterogeneities and fluctuations. If such fluctuations are correlated, they contribute to shear even if they vanish on average. In particular, the tensor D_{ij} includes shear stemming from correlations between triangle rotations and triangle elongation as well as correlations between triangle area changes and triangle elongation (Etournay et al., 2015; Merkel et al., 2017). Note finally that all the tensors introduced in Eqs. (3) and (4) are two-dimensional *nematic* tensors. It means that they are symmetric traceless tensors which are fully characterized by two independent quantities: a norm and an angle with respect to the x-axis (see also App. C4).

The choice of the triangulation affects how the total tissue shear rate $\widetilde{V}_{ij}$ is decomposed into the different cellular contributions. As we show below in a concrete example, the cell elongation contribution DQ_{ij}/Dt is only weakly affected by the choice of triangulation. However, the decomposition of R_{ij} into cellular contributions (Eq. (4)) depends crucially on the triangulation chosen (see Fig. 2). In particular, the *subcellular* triangulation yields by definition a vanishing T1 transition contribution: $T_{ij}^{\mathrm{sub}}=0$, as illustrated in Panel D of Fig. 2 and demonstrated in App. B. Compared to the dual lattice triangulation, the contribution of T1 events to the shear is transferred to the correlation term D_{ij} such that the sum $T_{ij} + D_{ij}$ contributing to R_{ij} remains essentially the same for both triangulations.

Note that the trace of the velocity gradient tensor V_{kk} (summation over repeated indices is implied), which corresponds to isotropic tissue growth, can also be decomposed into cellular contributions (Merkel et al., 2017; Popović et al., 2017). Here, we only focus on the anisotropic contributions. Finally, the tissue stress tensor Σ_{ij} in the simulations is symmetric and can be decomposed into an isotropic pressure and a symmetric traceless part, the shear stress $\widetilde{\Sigma}_{ij}$.

3.2. Shear decomposition of a polygonal network under pure shear

We now illustrate the shear decomposition procedure in the case of a cellular network under pure shear. Starting from an isotropic steady state of the cellular network at t=0, a pure shear boundary condition with constant shear rate $\widetilde{V}_{xx} = V_0$ along the x-axis is imposed on the network during a finite period, after which the box dimensions are fixed, and the system relaxes towards an isotropic steady state. See Movie 4 for illustration. In Fig. 3, we decompose the pure shear deformation into cellular contributions, using a dual lattice triangulation (panel A) and a subcellular triangulation (panel B).

Under pure shear, the tissue is characterized at short time by an elastic behavior as cells respond to the deformation by elongating (green curves in panels A and B). With a delay, cell elongation is then relaxed through T1 transitions (red curve in panel A), showing a viscous behavior of the cellular network at longer times. After a time $t \simeq 2$, we observe that the shear due to cellular rearrangements (red curve in panel A, purple curve in panel B) accounts for most of the pure shear and the mean cell elongation levels off. When shearing stops at t=6, topological rearrangements relax the cell elongation and the tissue reaches an isotropic steady state.

Note that the contribution to shear by cell rearrangements is captured by different terms of the shear decomposition (3) depending on the triangulation used. We focus here for simplicity on cell networks that undergo shear at constant cell number. This implies that a few division events occur that compensate occasional cell extrusions. Therefore, $C_{ij} \simeq 0$, $E_{ij} \simeq 0$ and $R_{ij} \simeq T_{ij} + D_{ij}$ to good approximation. Indeed, in the subcellular triangulation, this viscous behavior is not captured by the T1 transition contribution – which always vanishes in such triangulations –

[2] Note that the vertex needs not lie inside its associated triangle.

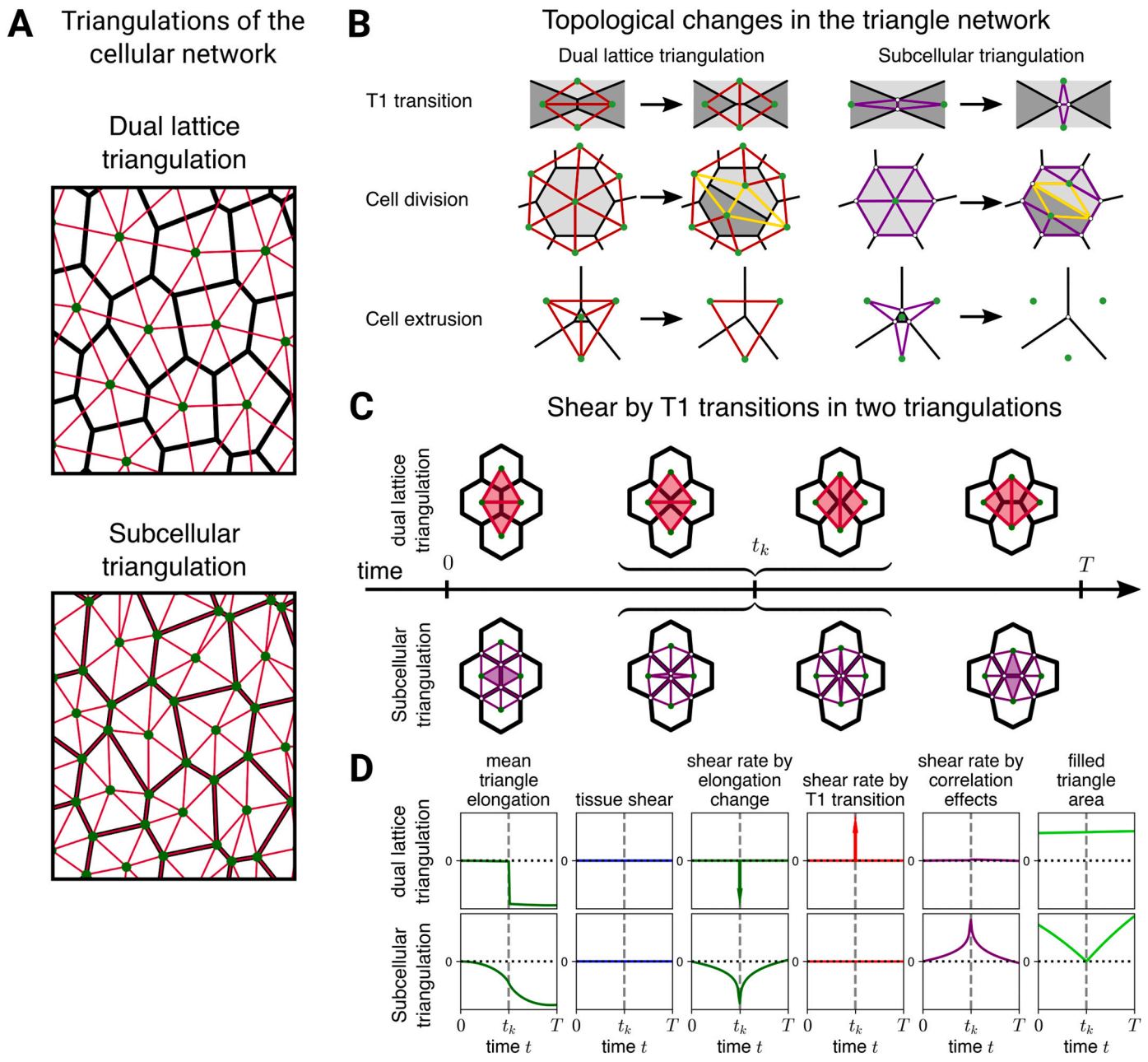

Fig. 2. Quantifying cellular contributions to tissue shear using two different triangulations. (A) Definitions of the two triangulations (red) of the cellular network (black). Top: Dual lattice triangulation, where the cell centers (green points) of neighboring cells are connected. Bottom: Subcellular triangulation, connecting each cell center with two consecutive vertices on the cell boundary. (B) Topological rearrangements in the dual lattice triangulation (left column, red triangles) and subcellular triangulation (right column, purple triangles) due to a T1 transition (top), cell division (middle) and cell extrusions (bottom). (C) Illustration of the shear rate contributions during a T1 transition using a dual lattice triangulation (top) or a subcellular triangulation (bottom). Between times 0 and t_k, the length of the central vertical bond is imposed to shrink to zero, at which point the topology of the cell network is changed. From t_k till T, the length is imposed to grow in the horizontal direction. See also Movies 2 and 3 for illustration. (D) For the process shown in (C), from left to right, the mean cell elongation, the total shear, shear due to cell shape change, shear due to T1 transitions, shear due to correlation effects and the mean area of the colored triangles in (C). See App. B for details.

but by the correlation contribution (purple curve in panel B). Importantly, adding the shear due to T1 transitions and the shear due to correlation effects in either of the two triangulations yields essentially the same contribution due to rearrangements, see the inset of panel B. In the following sections, we use the dual lattice triangulation when performing the shear decomposition in the vertex model. We only use the sum $T_{ij} + D_{ij}$ for comparison with the continuum model introduced in the next section. This comparison is insensitive to the triangulation used.

3.3. Comparison to a linear continuum model

The viscoelastic behavior of stochastic cellular networks can be captured by a continuum model of tissues. Such a coarse-grained description does not hold at a single cell level but requires an averaging over many cells, as provided by the shear decomposition of a triangulated network discussed above. We describe in this section how the decomposition of tissue shear is captured in a continuum model (Etournay et al., 2015; Marmottant et al., 2009; Popović et al., 2017). In

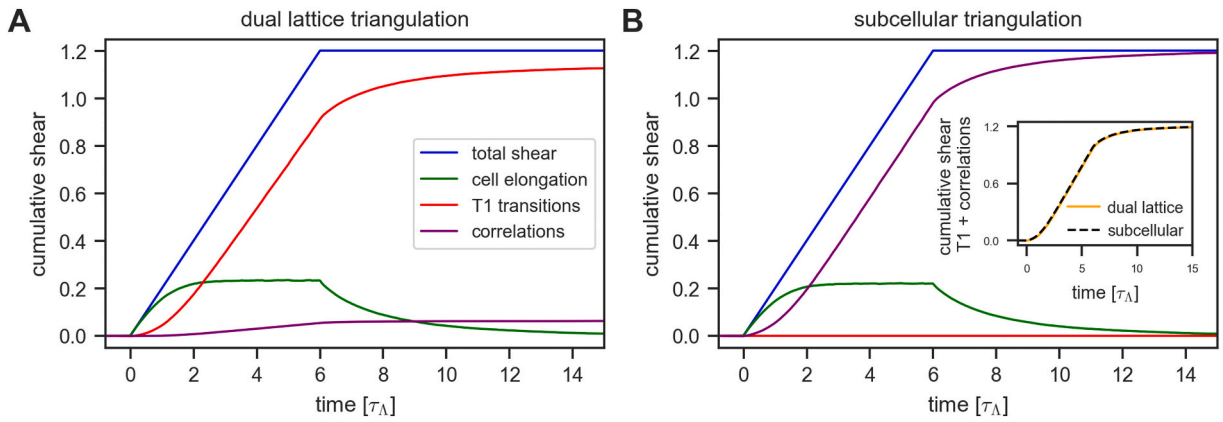

Fig. 3. Dynamics of an isotropic cellular network under an imposed pure shear deformation. From $t = 0$ to $t = 6$, we apply pure shear to the network with a rate $\widetilde{V}_{xx} = 0.2$, after which we let the system relax while keeping the box fixed. Panels show cumulatives of the total tissue shear (blue), decomposed in contributions to the shear due to changes in cell shape (green), due to T1 transitions (red) and due to correlation effects (purple). (A) Shear decomposition using a dual lattice triangulation or (B) subcellular triangulation. The inset in (B) shows the sum of the shear by T1 transitions and correlation effects, which gives a similar result for both triangulations. Vertex model parameter values used given in Table I (see Supplementary material). The data is averaged over 100 realizations of the vertex model. The standard error of the mean is smaller than the thickness of the curves.

all cases below, we discuss two-dimensional tissues, but the equations can be generalized to other dimensions.

3.3.1. *Cellular contributions to tissue deformation and tissue stress*

Similar to the shear decomposition performed for cell networks in Eq. (3), the anisotropic part of the deformation rate tensor $\widetilde{v}_{ij}$ can be decomposed into cellular contributions due to changes in the mean cell elongation tensor q_{ij} and shear r_{ij} caused by topological rearrangements. Note that we use lower-case letters for the continuum model description. We therefore have:

$$\widetilde{v}_{ij} = \frac{\mathrm{D}q_{ij}}{\mathrm{D}t} + r_{ij}, \tag{5}$$

where $\mathrm{D}/\mathrm{D}t$ denotes the corotational derivative defined in Eq. (C3) of the Supplementary material. We also introduce the tissue stress σ_{ij}, which we decompose into an isotropic part and an anisotropic symmetric traceless part, the tissue shear stress $\widetilde{\sigma}_{ij}$.

3.3.2. *Linear continuum model of an isotropic network*

We consider that the cellular network is an elastic material. To linear order, the shear stress is thus proportional to cell elongation and reads:

$$\widetilde{\sigma}_{ij} \simeq \mu_s q_{ij}, \tag{6}$$

where μ_s is the shear modulus of the tissue. In addition to this elastic response of the cellular network, which links stress to cell elongation, we also include in our continuum description the fact that the axis of cell elongation biases the axis of topological rearrangements. This fact is captured by introducing a linear relationship between the shear contribution from topological rearrangements r_{ij} and the cell elongation q_{ij}. It reads:

$$r_{ij} \simeq k_1 q_{ij}, \tag{7}$$

where k_1 is the characteristic rate of oriented topological rearrangements. This rate also plays the role of the inverse stress relaxation time of the viscoelastic tissue. The continuum shear decomposition Eq. (5) together with the constitutive equations (6) and (7) define material properties which are equivalent to a Maxwell fluid. Indeed, the stress obeys the following relation to shear rate:

$$\left(1 + \tau \frac{\mathrm{D}}{\mathrm{D}t}\right) \widetilde{\sigma}_{ij} = \eta \widetilde{v}_{ij}, \tag{8}$$

where the relaxation time is $\tau = 1/k_1$, and the tissue viscosity is $\eta = \mu_s/k_1$. A Maxwell fluid is a viscoelastic fluid with a single relaxation time τ. At short time ($t \ll \tau$), it behaves as an elastic solid with shear modulus μ_s and it flows at long time scales ($t \gg \tau$) as a viscous fluid with viscosity η. Recent experiments of migrating Madin–Darby canine kidney (MDCK) epithelial cell layers suggests that these tissues could behave as a viscoelastic Maxwell fluid with a relaxation time $\tau \simeq 70$ min (Tlili et al., 2020). As we will discuss in the following section, this linear description of the topological rearrangements given by Eq. (7) does not fully capture the rheological properties of cellular networks when tissue shear is high and the bond tension fluctuations are low and will need to be extended.

In Fig. 4, panel A, we compare the solution of the linear continuum model (solid lines) with the shear decomposition of the vertex model simulations (crosses). The tissue cell elongation $q_{ij}(t)$ is obtained by solving Eqs. (5) and (7), together with a pure shear boundary condition setting $\widetilde{v}_{ij}(t)$. The stress is then obtained using Eq. (6). The continuum model solution $q_{ij}(t)$ is given in Eq. (D6) in the Supplementary material and is used to fit the average cell elongation Q_{ij} quantified in the vertex model simulations. We have added the shear contributions due to T1 transitions and correlation effects ($T_{ij} + D_{ij}$) obtained from the vertex model simulations, and we compare their combined contribution to the rate of topological rearrangements r_{ij} in the continuum model.

We find that the linear continuum model with two fitting parameters k_1 and μ_s gives an accurate description of the observed shear flows in the vertex model for this choice of parameters and shear rate.

To test the limitations of the linear model, we now compare the continuum model results to the vertex model simulations for a higher shear rate. In the panel B of Fig. 4, we give the shear decomposition of the vertex model simulations (crosses) for an applied shear rate that is four times larger compared to panel A, and we compare it with the linear continuum model results (solid lines) using the values for μ_s and k_1 that were fit for in panel A. The linear model now overestimates the observed mean cell elongation in the vertex model, suggesting that the values of μ_s and k_1 would have to be changed for a better correspondence between both descriptions of the cellular network.

In the following, we will show that this limitation of the linear model can be addressed by the description of the tissue as a *nonlinear* active material. These nonlinearities in the vertex model are all the more pronounced when the bond tension fluctuations are low, as the system will be shown to behave more like a yield-stress material than a regular fluid (Bonn et al., 2017; Popović et al., 2021). We therefore focus in the next section on the influence of these fluctuations on the steady-state

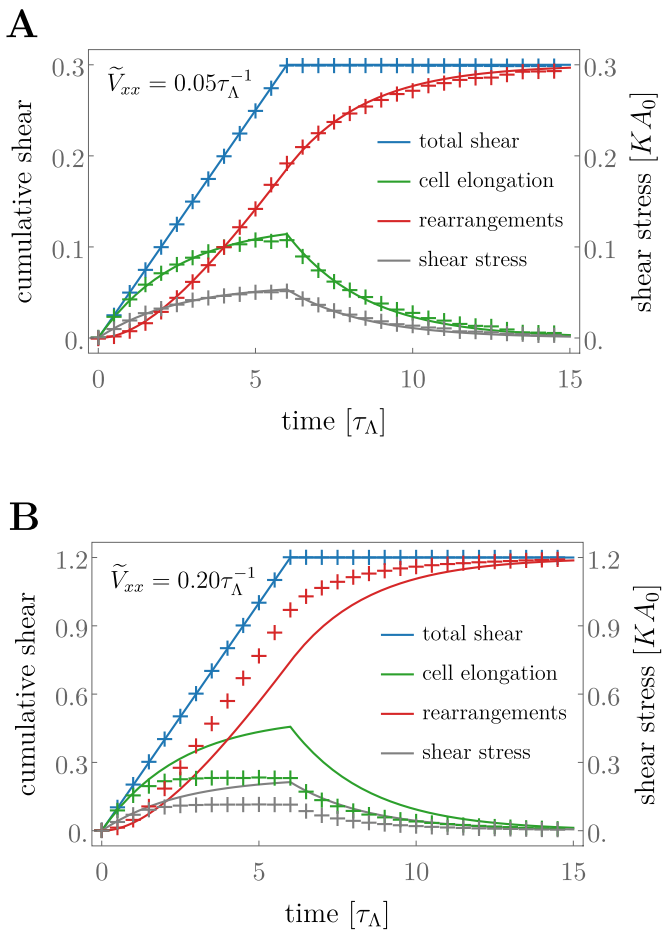

Fig. 4. (A) Fit of the isotropic continuum model (solid lines) to the shear decomposition of the cellular network dynamics of the vertex model (crosses, data from Fig. 3). A pure shear deformation is imposed along the x-axis with a rate $\widetilde{V}_{xx} = 0.05\tau_\Lambda^{-1}$. The shear due to rearrangements in the cellular network (dark red crosses) is obtained by adding the shear due to T1 transitions and correlation effects. Fit consists of two parts: (i) deformation under imposed pure shear and (ii) relaxation back to the isotropic state, where we use the parameter values, μ_s=0.47KA_0, k_1=0.40τ_Λ^{-1}. (B) Same setup as in panel A, but with a larger imposed shear rate $\widetilde{V}_{xx} = 0.20\tau_\Lambda^{-1}$. The values of μ_s and k_1 of the continuum model are the same as used in panel A. Note that we could have obtained a good fit if we did change the parameter values.

behavior of the vertex model.

4. Nonlinear rheology of cellular networks

In this section we continue on to explore the nonlinear properties of the vertex model. For this purpose, we investigate the effect of line tension fluctuations $\Delta\Lambda$ (see Eq. (2)) on the rheology of cellular networks. At vanishing fluctuation amplitude, the vertex model has been shown to behave as a yield-stress material (Popović et al., 2021), with a viscosity that diverges as the shear rate approaches zero. We observe that signatures of this zero-noise yielding transition can also be seen at finite values of the fluctuations and appear in terms of nonlinear rheology of the model tissue. Even at large noise strength, where a large number of T1 transitions occur and fluidify the system, we observe that the vertex model does *not* behave as a linear fluid but rather exhibits a shear-thinning behavior. Nonlinearities and in particular shear-thinning behavior have also been reported in a 3D version of the vertex model used to study the anisotropy of Kupffer's vesicle in zebrafish embryo (Sanematsu et al., 2021). Hints of rheofluidification have also been observed in experiments of migrating MDCK epithelial cell layers (Tlili et al., 2020). As we show below, these rheological properties of the vertex model can be captured by a continuum model with nonlinear material properties.

4.1. Shear thinning and nonlinear rheology in an isotropic polygonal cell network

Here we characterize the effect of line tension fluctuations on the shear flow in an isotropic cellular network. To this end, we study for different magnitudes of the line tension fluctuations $\Delta\Lambda$ the dependence of the steady-state cell elongation on simple shear.

In Fig. 5, panel A, we display the response of the steady-state mean cell elongation Q_{xy}^{ss} to the imposed rate of a simple shear deformation $\widetilde{V}_{xy}$, for different values of the magnitude of line tension fluctuations $\Delta\Lambda$. Filled symbols correspond to vertex model simulations and dotted lines correspond to a fit of a nonlinear model discussed below. We emphasize that the magnitude of the steady-state tissue shear stress, $|\widetilde{\mathbf{\Sigma}}^{ss}| = \sqrt{\left(\widetilde{\Sigma}_{xx}^{ss}\right)^2 + \left(\widetilde{\Sigma}_{xy}^{ss}\right)^2}$, is directly proportional to the magnitude of the steady-state mean cell elongation $|\mathbf{Q}^{ss}| = \sqrt{\left(Q_{xx}^{ss}\right)^2 + \left(Q_{xy}^{ss}\right)^2}$, see panel B. As a consequence, panel A can be read directly as a shear stress versus shear rate plot, from which the rheological properties of cell networks can be discussed.

A first observation is shear thinning: the viscosity of the cellular network is lower at higher shear rates, since the slope of the response of tissue mean cell elongation to the applied shear rate decreases at higher shear rates (see Fig. 5A). This can be understood qualitatively by observing that to accommodate an imposed shear rate, cells in the network elongate but more importantly must undergo T1 transitions. As the shear rate increases, the rate of T1 transitions increases because additional transitions are driven by the extra shear. These T1 transitions keep the cell elongation at a smaller level. Since the tissue stress is proportional to cell elongation, a shear-thinning behavior follows.

Second, our results suggest a stronger nonlinear behavior at low noise magnitude. We observe a glassy behavior in this regime, indicated by a large viscosity at small values of the imposed shear rate, which is then followed by a shear-thinning a larger shear rates (see Fig. 5A). As long as the fluctuation magnitude is finite, the vertex model does *not* have a yield stress, and the steady-state cell elongation vanishes at vanishing shear rate (see the inset in Fig. 5A). These steady states are however reached for longer and longer time scales as the shear rate is lowered and as the bond fluctuation magnitude is lowered. This glassy behavior is the signature of the yielding transition that exists in the vertex model at vanishing bond tension fluctuation magnitude (Popović et al., 2021).

Finally, large shear rates correspond to dynamics which are fast compared to the bond tension fluctuation time scale. For sufficiently large shear rates, the bond dynamics can therefore be considered as frozen and we enter a regime which is equivalent to the quasistatic limit discussed for instance in Popović et al., 2021. Interestingly, a signature of the bond tension fluctuations will still be observable as the state of the system will depend on the frozen distribution of bond tension magnitudes.

The cell elongation reaches at large shear rate a plateau value that corresponds to the quasistatic limit. At small bond tension fluctuation magnitude ($\Delta\Lambda/\Lambda_0 \simeq 0.20$), this plateau can be seen in Fig. 5A. At larger bond tension fluctuation magnitude ($\Delta\Lambda/\Lambda_0 \simeq 0.50$ for instance), larger shear rates are required before the bond tension can be considered frozen and the corresponding plateau is reached at larger shear rate. A more thorough scaling analysis of the crossover between fluctuation-driven dynamics and quasistatic behavior is beyond the scope of this

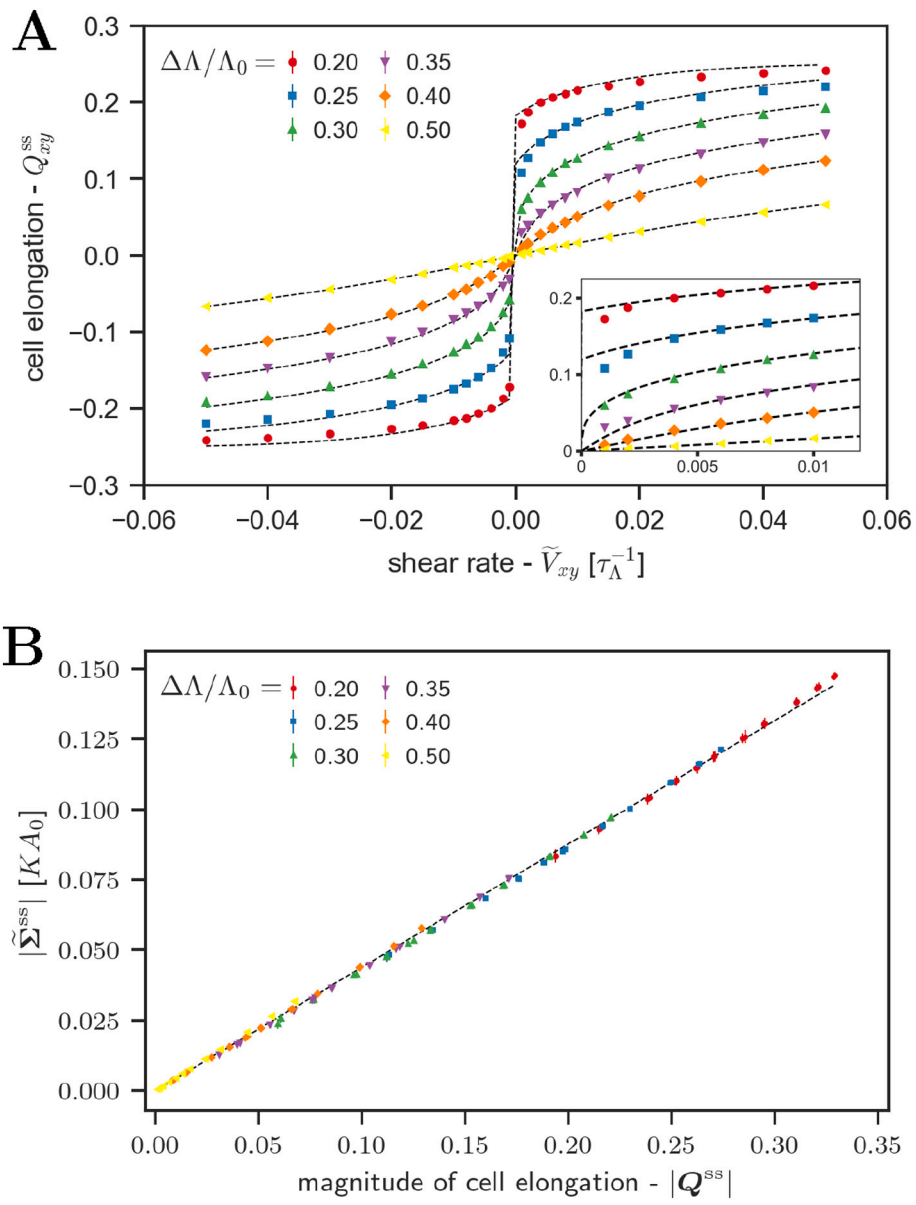

Fig. 5. Nonlinear response of the isotropic cellular network to different rates of imposed simple shear deformation. The color of the symbols indicate different values used for the magnitude of the line tension fluctuations in the simulations, $\Delta\Lambda$, which are given in the legend. (A) Steady state value of the xy-component of the mean cell elongation tensor Q^{ss}_{xy} against the imposed simple shear rate, $\widetilde{V}_{xy}$. Dashed black lines show separate fits of the nonlinear continuum model in Eq. (9) for each value of $\Delta\Lambda$. Fitted values for k_1 and k_3 are given in Table II (see Supplementary material). The xx-component of the mean elongation tensor are given in Figure S1 (see Supplementary material). Inset highlights the data at small positive shear rates. (B) Magnitude of the steady-state shear-stress tensor against the magnitude of the mean cell elongation. The color of the symbols correspond to the values of $\Delta\Lambda$. Different symbols of the same color correspond to different applied shear rates. The dashed line corresponds to a linear fit (including the origin) through all the data points. The tissue elastic shear modulus μ_s=0.44 is given by the slope of this linear fit. Each data point has been obtained by averaging over 25 realizations of the vertex model. The standard error of the mean is smaller than the marker size.

paper.

4.2. Nonlinear continuum model of an isotropic network

We have discussed in Section 3.3.2 a description of tissues with material properties that depend linearly on the tissue state (see Eqs. (6) and (7)). This linear model predicts a linear response of the mean cell elongation to small values of the applied shear rate and a vanishing cell elongation as the shear rate approaches zero, see App. D2. However, such a linear model does not agree with what we observe in the vertex model simulation of the cellular network, as discussed above and shown in Fig. 5, especially for lower values of the magnitude of the line tension fluctuations. In the low line tension fluctuations regime, the linear elastic behavior of the tissue stress as a function of cell elongation, $\widetilde{\sigma}_{ij} = \mu_s q_{ij}$, is expected to remain valid, as suggested by panel B of Fig. 5. However, the fluctuation magnitude is expected to play a crucial role in the rate of topological rearrangements: at low magnitude, rearrangements triggered by bond tension fluctuations occur extremely rarely, inducing the appearance of a glassy regime at vanishing shear rate.

Therefore, we expand the linear constitutive equation for the rate of rearrangements tensor r_{ij}, with the lowest-order nonlinear dependence on the cell elongation tensor allowed by the symmetry of the system. Using the fact that r_{ij} is a symmetric traceless tensor, we thus write the nonlinear constitutive equation:

$$r_{ij} = k_1 q_{ij} + \frac{k_3}{2}\mathrm{Tr}[\boldsymbol{q}\cdot\boldsymbol{q}]q_{ij}, \tag{9}$$

where k_3 is a rate for the third-order dependence of r_{ij} on cell elongation. Note that this simple form is obtained in two dimensions, where the square of a symmetric traceless tensor is always proportional to the identity: $\boldsymbol{q}^2 = q^2\mathbb{1}$, where $q = \sqrt{q_{xx}^2 + q_{yy}^2}$ is the norm of the nematic tensor and $\mathbb{1}$ is the identity matrix in two dimensions. In three dimensions, an additional term would need to be considered. The results shown in Fig. 5B reveal that Eq. (6) does not need to be extended to nonlinear order.

The nonlinear material properties given by the constitutive equation (9) can first be used to obtain the dynamics of the cell elongation and cell

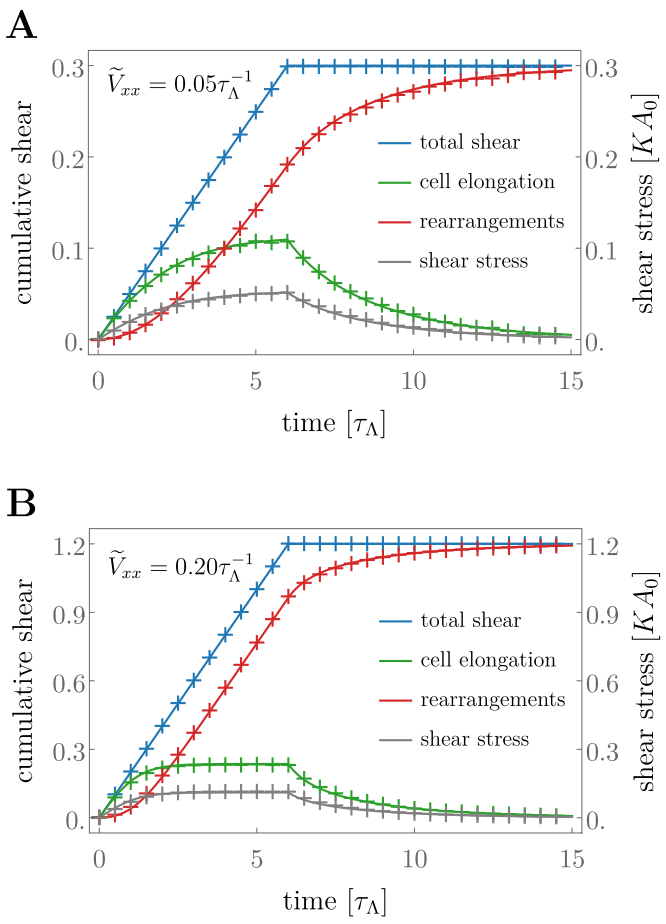

Fig. 6. Nonlinear fit (solid lines) to the shear decomposition of the cellular network dynamics of the vertex model (crosses, data from Fig. 3). (A) A pure shear deformation is imposed along the x-axis with a rate $\widetilde{V}_{xx} = 0.05\tau_\Lambda^{-1}$. (B) Same setup as in panel A, but with a larger imposed shear rate $\widetilde{V}_{xx} = 0.2\tau_\Lambda^{-1}$. The same fit parameters k_1=0.32 and k_3=4.72 have been used for both panels, hence solving the limitation of the linear model displayed in Fig. 4. Note that the best fit for the shear stress (gray curves) is obtained with μ_s=0.47KA_0, which is the same value as in Fig. 4.

rearrangements of a cell network under pure shear. The nonlinear fit to the same data as in Fig. 4 leads to an excellent agreement with the simulation results using only two fit parameters that are the same for both shear rates, see Fig. 6. In addition to providing a better agreement with the data, the nonlinear model solves the limitation of the linear model, which did not provide a satisfying fit for two different shear rates if the same parameters where used.

We then use the nonlinear constitutive Eq. (9) to obtain the behavior of a cell network under simple shear. We can in particular determine the steady-state cell elongation q_{ij}^{ss} in the network as a function of the imposed shear rate v_0, as presented in App. D3. We fit the resulting expression for q_{ij}^{ss} to the simulation data given in Fig. 5. We find an excellent agreement between the nonlinear continuum model and the simulation data, both at high and low levels of line tension fluctuations.

At large bond tension fluctuation magnitude, the continuum model captures well the rheological properties of the vertex model and in particular its shear-thinning behavior (see the dotted lines fitting the yellow, orange, purple and green dots in Fig. 5). At low level of bond tension fluctuations and for small shear rates, the vertex model does not have a yield stress but does exhibit the glassy behavior mentioned above. This glassy regime is not captured by the continuum model but is reflected in a yield stress that arises for negative values of the coefficient k_1 (see the dotted lines fitting the blue and red dots in Fig. 5). Indeed, as discussed in App. D3, the steady-state elongation for the continuum model has the following behavior at low shear rate:

$$q_{xy}^{ss} = \begin{cases} \dfrac{v_0}{k_1} + \mathscr{O}(v_0^2) & \text{if } k_1 \geq 0, \\ \pm\dfrac{\sqrt{-k_1(2k_1+k_3)}}{\sqrt{2}k_3} - \left(\dfrac{2}{k_3} + \dfrac{1}{2k_1}\right)v_0 + \mathscr{O}(v_0^2) & \text{if } k_1 < 0, \end{cases} \tag{10}$$

where the $\pm$ sign corresponds to positive and negative shear rates, respectively. When k_1>0, Eq. (10) shows that the low shear rate behavior of the fluid is that of a simple viscous liquid with viscosity $\eta = \mu_s/k_1$. For k_1<0, the low shear rate behavior of the fluid corresponds to that of a Bingham fluid (Steffe, 1996) with a yield stress $\sigma_{xy}^{y} = \mu_s\sqrt{-k_1(2k_1+k_3)}/\sqrt{2}k_3$ and a viscosity $\eta' = -\mu_s(1/(2k_1) + 2/k_3)$>0. Note that Eq. (10) describes the linear regime of the continuum model rheology shown in Fig. 5.

Negative k_1 are found by our fits to the simulation data in situations where the rheology is effectively captured by a yield stress in simulations run over finite time intervals and finite shear rates. Note, however, that the vertex model does not have a yield stress if simulations are run over long times. Such an apparent yielding behavior is observed in our simulations below $\Delta A_c \simeq 0.3A_0$. To fully capture the glassy regime at low line tension fluctuations and low shear rates requires a more detailed analysis that is beyond the scope of the present paper (Popović et al., 2020; Matoz-Fernandez et al., 2017).

4.3. Rheology of a network with anisotropic active cell stress

So far we have discussed the nonlinear properties of an isotropic cellular network, in which the ground state is a regular hexagonal network, without a preferred axis. We now discuss the rheology of an anisotropic tissue. The anisotropy of the network is associated with a nematic

$$\mathscr{P}_{ij} = 2P_iP_j - \delta_{ij}, \tag{11}$$

assigned to each polygon, which is constructed from a unit polarity vector P_i, motivated by planar cell polarity (Bosveld et al., 2012; Wang and Nathans, 2007). In two dimensions, this nematic can be parameterized by a single angle Ψ which defines the direction of the anisotropy axis (see App. C4 for details). Although the polarity field may change with time and may depend on cell stress, we consider for simplicity that Ψ is constant in the following. Moreover, this nematic field gives rise to anisotropic active stresses in the tissue. In the vertex model, this is implemented by adding the work performed by this active stress Σ_{ij}^a to the vertex model work function, which reads:

$$W = W_0 - \sum_\alpha \frac{1}{2}A^\alpha \Sigma_{ij}^a G_{ij}^\alpha, \tag{12}$$

where W_0 is defined in Eq. (1) and G_{ij}^a is the cell shape tensor of each cell α

$$\mathbf{G}^\alpha = \frac{1}{A^\alpha}\sum_{\langle mn\rangle}\widetilde{\mathcal{L}}_{mn}. \tag{13}$$

Here, $\widetilde{\mathcal{L}}_{mn}$ is a symmetric traceless tensor defined by the orientation of the bond connecting vertices m and n. From the vector $\mathcal{L}_{mn}$ pointing from vertex m to vertex n, we define $\widetilde{\mathcal{L}}_{mn} = \mathcal{L}_{mn}\otimes\mathcal{L}_{mn} - \frac{1}{2}\mathcal{L}_{mn}^2\mathbb{1}$ where $\otimes$ is the tensor product. The cell shape tensor $G_{ij}{}^\alpha$ quantifies the deviation of the cell shape from isotropic shapes, for which $G_{ij}{}^\alpha$=0. See Fig. 1 for an illustration. The direction of the anisotropic active stress is set by the cell nematic as $\Sigma_{ij}^a = \Sigma^a\mathscr{P}_{ij}$, where Σ^a is the magnitude of the active stress. Note that with this definition and $\Sigma^a > 0$, this additional anisotropic stress is extensile along the axis set by $\mathcal{P}_{ij}$. Other conventions can also be used. See Movie 5 for an illustration of the dynamics of the vertex model

in presence of an anisotropic stress. Note that anisotropy in the system in general could also be caused by anisotropic bond tensions and bond tension fluctuations. This will be the subject of a separate paper (Duclut et al., in preparation).

To characterize the effects of anisotropic active stress at an angle Ψ on the shear flow in cellular networks, we study the response of the mean cell elongation in the network to the rate of imposed pure shear. We vary the angle Ψ of the polarity axis $\mathscr{P}_{ij}$, while the direction of the imposed pure shear is kept along the x-axis. Then, starting from a steady-state network configuration under a fixed boundary condition, we apply a pure shear deformation along the x-axis, until the magnitude of the cell elongation tensor has plateaued, and then quantify the mean cell elongation tensor Q_{ij}^{ss}. We characterize this mean cell elongation tensor by its magnitude $|\boldsymbol{Q}^{ss}|$ and the angle of orientation of its axis Φ^{ss} (see App. C4). As a consequence of the active anisotropic cell stress, the steady-state mean cell elongation tensor Q_{ij}^{ss} does not vanish even when the external shear is zero. To discriminate between the effect of the applied pure shear deformation and that of the active stress field, we define the norm $|\boldsymbol{Q}_0^{ss}|$ and orientation angle $\Phi_0^{ss} = \Psi$ of the elongation tensor for a vanishing external shear.

In Fig. 7, panels A and B, we show the perturbation of the magnitude $|\boldsymbol{Q}^{ss}| - |\boldsymbol{Q}_0^{ss}|$, and the perturbation of the axis direction $\Phi^{ss} - \Psi$ of the mean elongation tensor due to the applied shear. The results clearly show that the response of a cellular network to shear strongly depends on the angle between the applied deformation and the active stress. Under a nonzero pure shear rate the magnitude of cell elongation (panel A) has approximately a cosine dependence on the polarity angle, with strongest changes in the magnitude of elongation at the angles Ψ=0 and $\Psi = \pi/2$. The change in the angle of the elongation tensor due to the pure shear has approximately a sinusoidal dependence on Ψ, with maximal perturbations at $\Psi = \pi/4$ and Ψ=3π/4.

Importantly, for a shear rate $\tilde{V}_{xx} = 0.05$, the magnitude of elongation at Ψ=0 increases by about 0.06, while the magnitude at $\Psi = \pi/2$ decreases by about −0.08, revealing that the response is not simply a cosine. Such a behavior is not expected for a linear system and is a signature of the nonlinear response of the cellular network to the applied shear. To highlight this nonlinear response in the presence of an anisotropic active stress at an angle Ψ, we show in panel C of Fig. 7 the change in the magnitude of the mean cell elongation due to a small change in the imposed shear rate, evaluated at $\tilde{V}_{xx} = 0.025\tau_\Lambda^{-1}$. We find that the mean cell elongation in the tissue is more sensitive to changes in the shear rate when the active stress is oriented perpendicular to the axis of pure shear ($\Psi = \pi/2$) as compared to the case when it is oriented parallel to the axis of pure shear (Ψ=0).

This nonlinear response of the vertex model can be understood as follows. The active stress axis sets the preferred axis for cell elongation in the absence of shear (see Movie 5 for illustration). When an external shear is applied along the x axis, cells that are already elongated in the x direction (Ψ=0) keep elongating in this direction (see Fig. 7A for Ψ=0), while cells elongated in the y direction ($\Psi = \pi/2$) become more isotropic. See Fig. 8 for a schematic illustration. If the cellular network was a linear material, elongating the already anisotropic cells or decreasing their elongation would have a symmetric effect. However, nonlinearities stemming from the vertex model geometry challenge this linear picture. At a given shear rate, cells of the vertex model are more easily deformed to an isotropic shape than to a more anisotropic shape, as illustrated by the fact that the curves in panel A and C of Fig. 7 are not symmetric cosines. We show below and in App. D4 that this behavior of the vertex model cannot be obtained in a *linear* continuum model, but is accurately captured by our *nonlinear* continuum model. Interestingly, this picture also suggests that convergence-extension of tissues (Wang et al., 2020; Rauzi et al., 2010) could be facilitated or triggered by an anisotropic stress pattern in the tissue.

4.4. Nonlinear continuum model of network with active stress

To capture the nonlinear response of the network to a combination of external pure shear and active cell stress presented in Fig. 7, we extend the isotropic material properties for the rate of rearrangements r_{ij} as given by the constitutive equation (9) to the case of an anisotropic material. This anisotropy is captured by the nematic field p_{ij}, which is the continuum model equivalent of $\mathscr{P}_{ij}$. In the presence of this additional anisotropy, the most general constitutive equation for the traceless symmetric tensor r_{ij} in two dimensions reads:

$$r_{ij} = k_1 q_{ij} + \Big(\lambda_0 + \frac{\lambda_1}{2}\mathrm{Tr}[\boldsymbol{p}\cdot\boldsymbol{q}] + \frac{\lambda_2}{2}\mathrm{Tr}[\boldsymbol{q}\cdot\boldsymbol{q}] + \frac{\lambda_3}{2}\mathrm{Tr}[\boldsymbol{p}\cdot\boldsymbol{q}\cdot\boldsymbol{p}\cdot\boldsymbol{q}]\Big) p_{ij} + \delta_0\, p_{ik}q_{kl}p_{lm}q_{mn}p_{nj} + \mathcal{O}(|\boldsymbol{q}|^3)\,, \tag{14}$$

where we have considered the lowest nonlinear terms in the cell elongation $\boldsymbol{q}$. Importantly, note that these lowest-order nonlinear terms are of order two in $\boldsymbol{q}$, whereas they were of order three in the isotropic case (see Eq. (9)). Contributions of order two do not exist in the isotropic case because $\boldsymbol{q}^2 \propto \mathbb{1}$ (in spatial dimension d=2), while they do exist in the presence of the anisotropic order parameter $\boldsymbol{p}$. In addition, we also need to add linear anisotropic terms to the stress constitutive Eq. (6), see App. D4c.

In order to obtain a closed expression for q_{ij} and to fit it to the mean cell elongation Q_{ij} obtained from the vertex model simulations, we parameterize the elongation tensor by its norm $q = |\boldsymbol{q}|$ and orientation angle ϕ (see App. C4). Writing $\phi = \psi + \delta\phi$, we expand the elongation

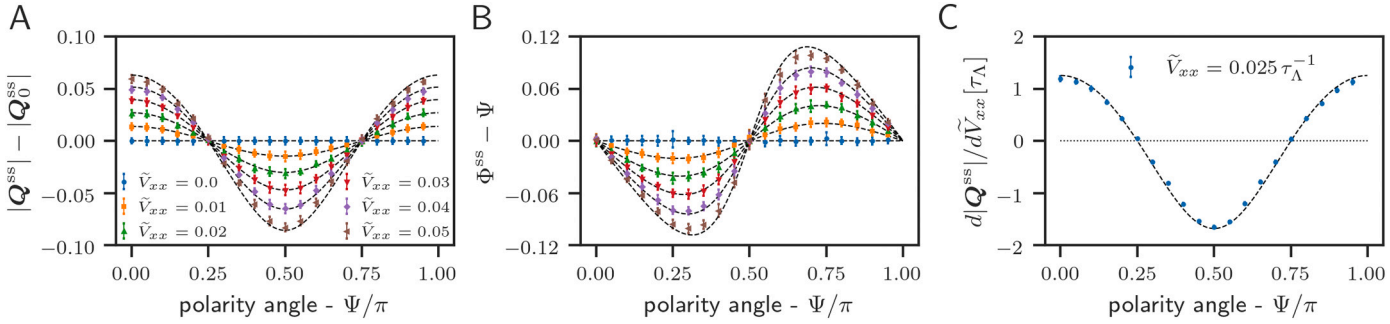

Fig. 7. Changes in the steady state mean cell elongation due to an imposed pure shear deformation in a cellular network with anisotropic cell stress, against the angle of the polarity axis, Ψ. In panels A and B, different colors correspond to different applied pure shear rates, given in the legend of panel A. Dotted lines show the fit of the nonlinear anisotropic model with the constitutive equation (14). (A) Change in the magnitude of the mean cell elongation due to pure shear $|\boldsymbol{Q}^{ss}|$, compared to the case when no shear is imposed, $|\boldsymbol{Q}_0^{ss}|$. (B) Change in the angle Φ^{ss} of the mean elongation tensor compared to the angle Ψ when no shear is imposed. (C) Susceptibility of the magnitude of cell elongation to changes in the applied shear rate. Derivative taken at $\tilde{V}_{xx} = 0.025\tau_\Lambda^{-1}$. Dotted lines give the prediction obtained from the nonlinear model of Section 4.4. Parameter values obtained from the fit given in Table III (see Supplementary material).

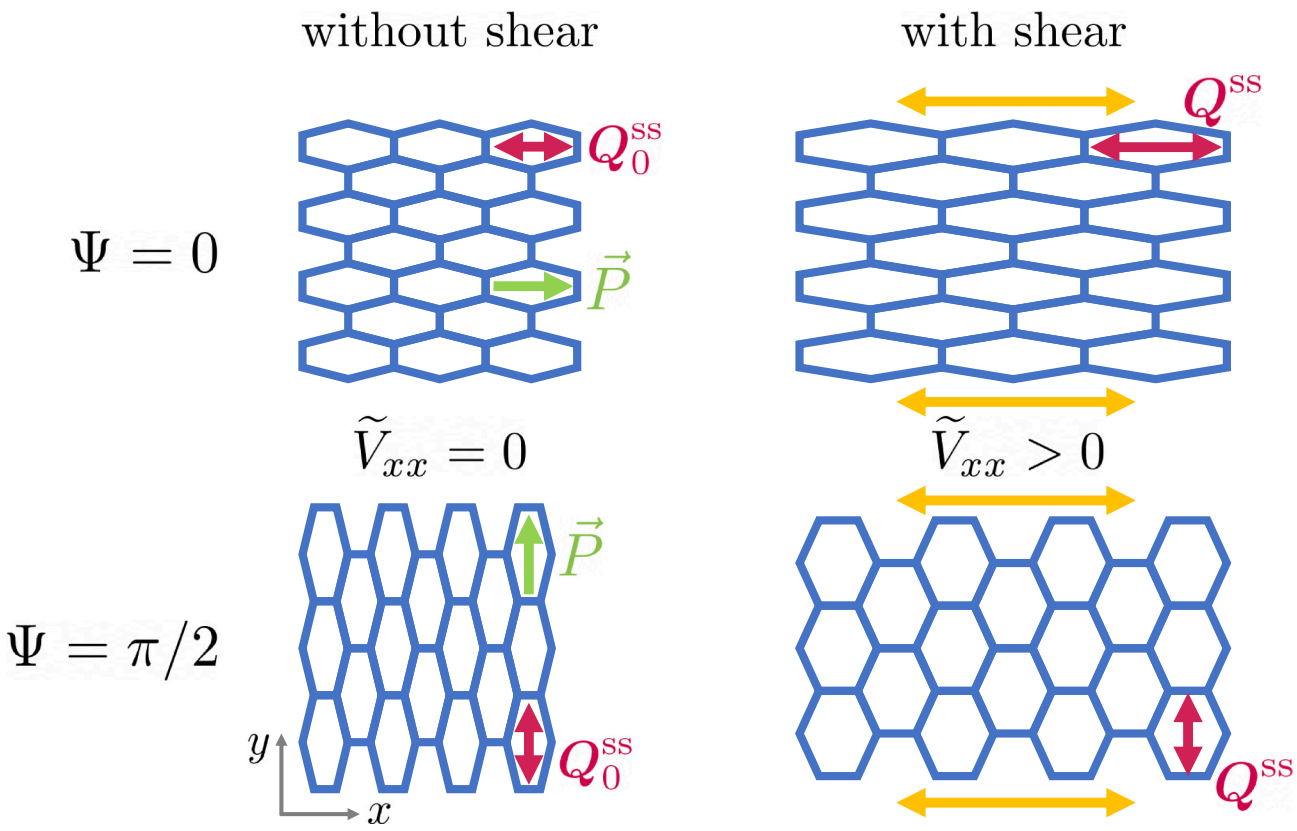

Fig. 8. Schematic illustration of the shearing of a cellular network in the presence of an anisotropic stress. (Top row) Cells are elongated in the x direction as a consequence of an anisotropic stress along the x axis (Ψ=0). Shear along the x direction accentuates cell anisotropy. (Bottom row) Cells are elongated in the y direction as a consequence of an anisotropic stress along the y axis ($\Psi = \pi/2$). Cells become more isotropic when sheared along the x direction.

tensor in $\delta\phi$. To linear order in $\delta\phi$, Eq. (14) then reads:

$$r_{ij}^{(1)} = [g(q)\,\delta_{ik} + 2\delta\phi\, h(q)\,\varepsilon_{ik}\,]p_{kj} + \mathcal{O}\left(\delta\phi^2\right), \tag{15}$$

where ε_{ij} is the fully antisymmetric tensor in two dimensions with $\varepsilon_{xy} = -1$, ε_{yx}=1 and $\varepsilon_{xx} = \varepsilon_{yy}$=0. Here we have introduced $g(q) = (\beta_2 q^2/2 + \beta_1 q + \lambda_0)$ and $h(q) = (\beta_4 q^2 + \beta_3 q + \lambda_0)$, where the effective parameters $\beta_{1,2,3,4}$ are given in Eq. (D29) of App. D4. We can now solve the steady-state shear decomposition with pure shear boundary conditions, $\tilde{v}_{ij} = r_{ij}^{(1)}$, to obtain a closed expressions for q and $\delta\phi$, see Eq. (D30) of App. D4.

Fig. 7, panels A and B, shows the fits of this continuum model to the vertex model data using Eq. (D30) of App. D4. Values of the fit parameters are given in Table III (see Supplementary material). We find that the nonlinear continuum theory agrees well with the data. This shows that the continuum model correctly captures the nonlinearities of the magnitude of mean cell elongation in response to changes in the shear rate, as shown in panel C. We emphasize that the non-symmetric behavior of the magnitude of mean cell elongation in response to changes in the shear rate cannot be obtained in a *linear* continuum model and requires nonlinear material properties (see App. D4 for details).

5. Discussion and conclusion

We have discussed the nonlinear rheology of cellular networks described by a vertex model. We have analyzed its rheology using a shear decomposition based on a triangulation method (Merkel et al., 2017), and have shown that the nonlinear properties of the cell network can be captured by a continuum model.

We have used two different triangulation schemes (dual lattice and subcellular) to show that these different choices lead to different definitions of contributions to shear by T1 transitions and by correlations. We show that the sum of both contributions, which we call the contribution from cell rearrangements, is independent of the choice of triangulation. The choice of triangulation cannot have a meaning in the continuum limit, and consistent with that fact we have shown that the cell rearrangement contribution is well-captured by the continuum theory. We also note that the subcellular triangulation can be especially useful to study epithelial tissues that are not planar as it provides a natural triangulation of the curved manifold.

Our exploration of the vertex model rheology has been performed in shear-rate regimes that are reasonable for biological tissues. Indeed, in a recent experiment of migrating Madin–Darby canine kidney (MDCK) epithelial cell layers (Tlili et al., 2020), a tissue shear rate of about 0.005 min^{-1} was reported. Similarly, Etournay et al., 2015 find shear rates of order $\simeq 2 10^{-2}$ $\text{h}^{-1} \simeq 3 10^{-4}$ min^{-1} during pupal wing morphogenesis. Taking the myosin turnover time $\tau_m \simeq 2$ min 22 s (Curran et al., 2017) as a proxy for the bond tension fluctuation persistence time τ_Λ, this corresponds in our dimensionless units to shear rates of the order of $v_0 \simeq 10^{-3} - 10^{-2}$.

The rheology of the cellular network is strongly governed by fluctuations. We have focused on a vertex model with bond tension fluctuations. Bond tension fluctuations lead to fluctuations of bond length, which can in turn trigger stochastic topological rearrangements in the network that can relax elastic stresses. Obtaining estimations for the bond tension fluctuation magnitude in biological tissues is challenging, and a precise quantification requires to carefully compare experimental and simulation data, for instance by comparing bond length distributions. Such a comparison has been performed in Curran et al., 2017. There, an estimate of $\Delta\Lambda/\Lambda_0 \simeq 0.3$ was reported for a slightly different model. In addition, it is important to emphasize that according to some recent results (for instance Mongera et al., 2018), bond tension fluctuation magnitude may vary spatially. It is thus relevant to theoretically

probe different fluctuations regimes. We also emphasize that we have focused our analysis on the parameter region where the vertex model is rigid and has a finite shear modulus (Bi et al., 2015; Farhadifar et al., 2007). Within this region, we expect our results to be qualitatively robust, even when the vertex model parameters differ from the values that we have chosen here. We have not explored the role of bond tension fluctuations in the *soft* region of the parameter space.

As a result of the stochastic topological rearrangements triggered by bond tension fluctuations, the cellular network can exhibit viscoelastic behavior with a characteristic relaxation time. Such viscoelastic behavior has been observed in the MDCK cell experiment discussed above (Tlili et al., 2020), and a linear Maxwell description was proposed with a characteristic time $\tau \simeq 70$ min for the relaxation of the elastic stresses was reported, which corresponds in our model to $k_1 = 1/\tau \simeq 0.014\ \mathrm{min}^{-1}$. For increasing shear rates, our model displays a nonlinear response in the steady-state stress which corresponds to shear thinning, and is well-captured by a cubic term in the continuum theory. A similar observation of rheofluidification was observed for MDCK cell layers, where decreasing values of the Maxwell relaxation time τ are obtained as the average cell velocity increases (Tlili et al., 2020). It remains for future work to explore whether our nonlinear continuum model can account for this observation. We also note that a shear-thinning behavior was observed in the context of a 3D Voronoi model designed to study the motion of the Kupffer's vesicle in zebrafish embryo (Sanematsu et al., 2021).

At low bond tension fluctuation strength, nonlinear effects become strong in our model, and the system exhibits a glassy behavior with large viscosity at small shear rate. Variations in the magnitude of bond tension fluctuations could therefore explain the differences in the rheological properties of tissues, as they have been for instance characterized in the case of tumor spheroids (Grosser et al., 2021). Cancerous spheroids have been reported to display a fluid-like behavior and can fuse like liquid droplets; healthy tissues on the other hand are more solid-like, and coalescence of healthy spheroids is arrested before complete fusion.

From a theoretical perspective, the nonlinear behavior of cell networks that we have discussed is a signature of the zero-noise yielding transition that is observed in the vertex model (Popović et al., 2021) and that remains pronounced at finite noise strength. In our mean-field continuum theory, this behavior is reflected by an apparent yield stress below a characteristic noise strength.

In our model, cell number is constant on average, and the contributions from cell divisions and extrusions to shear are small. As a consequence, the shear-thinning and other nonlinear properties that we report rely essentially on T1 transitions. However, it has been shown that cell divisions and extrusions can also fluidify a tissue and cause shear thinning (Ranft et al., 2010; Matoz-Fernandez et al., 2017). Hence, studying the combined effect of these different sources of cellular fluctuations will be especially relevant for biological tissues, where all these cellular events contribute significantly to the macroscopic rheological properties (Guirao et al., 2015; Etournay et al., 2015).

It will be an interesting challenge to relate the coefficients in the continuum theory to the parameters of the vertex model. One promising approach would be to derive equations for the distribution of bond lengths in the tissue in the presence of external shear and relate those to the macroscopic network behavior. Such approaches have recently been shown to be a valuable tool to investigate the rheological properties of the vertex model in the noiseless regime (Popović et al., 2021). Relating such approaches to experimentally determined cell bond length distribution in tissues could help understand the rheological properties of real tissues.

Nonlinearities can be systematically taken into account in the continuum theory based on symmetry arguments. This allowed us to generalize our approach to discuss the rheology of anisotropic cell networks. At the vertex model level, we have focused on an anisotropy that stems from a preferred axis, along which cells can exert active stresses. In addition, cell bond tension can be anisotropic, which can be studied in the same framework (Duclut et al., in preparation). In the presence of anisotropy, the rheological response depends on the angle between the axis of shear and the axis of anisotropy and exhibits interesting nonlinearities. We have shown that these features are well-captured by the nonlinear continuum theory. The consideration of such anisotropy is a first step to build an understanding of biological tissues, in which chemical signals such as planar cell polarity pathways (Bosveld et al., 2012; Wang and Nathans, 2007) can create large-scale patterns of tissue polarity, which can influence their mechanical and rheological properties, for instance by biasing the axis of cell division (Gho and Schweisguth, 1998). We have considered in our vertex model a *global* nematic anisotropy. In the future, it will be important to discuss the emergence of self-organization of such polarity via *local* signals (Aigouy et al., 2010; Sagner et al., 2012). Furthermore, spatially separated patches of cells have in general different mechanical properties and may present different anisotropy axes (Jain et al., 2020). This is the case, for example, in the *Drosophila* wing disc pouch, where cells along the dorsoventral axis are on average smaller and less elongated (Dye et al., 2020; Dye et al., 2017). Investigating the role of spatial dependence of tissue properties in developmental processes is an important challenge for future works.

Supplementary data to this article can be found online at https://doi.org/10.1016/j.cdev.2021.203746.

CRediT authorship contribution statement

C. Duclut, J. Paijmans, M. M. Inamdar, C. D. Modes, and F. Jülicher designed research, performed research, and wrote the paper.

Declaration of competing interest

The authors declare no conflict of interest.

Acknowledgements

We thank Marko Popović for enlightening discussions and for his useful comments on the manuscript. M.M.I. acknowledges funding from Science and Engineering Research Board (MTR/2020/000605) and the hospitality at MPI-PKS, Dresden. C.D.M and F.J. acknowledge funding by the Federal Ministry of Education and Research under grant number 031L0160.

References

Aigouy, B., Farhadifar, R., Staple, D.B., Sagner, A., Röper, J.-C., Jülicher, F., Eaton, S., 2010. Cell 142, 773.
Alt, S., Ganguly, P., Salbreux, G., 2017. Phil. Trans. R. Soc. B 372, 20150520.
Angelini, T.E., Hannezo, E., Trepat, X., Marquez, M., Fredberg, J.J., Weitz, D.A., 2011. Proc. Natl. Acad. Sci. U. S. A. 108, 4714.
Arraf, A.A., Yelin, R., Reshef, I., Jadon, J., Abboud, M., Zaher, M., Schneider, J., Vladimirov, F.K., Schultheiss, T.M., 2020. Dev. Cell 53, 589.
Atia, L., Bi, D., Sharma, Y., Mitchel, J.A., Gweon, B., Koehler, S.A., DeCamp, S.J., Lan, B., Kim, J.H., Hirsch, R., Pegoraro, A.F., Lee, K.H., Starr, J.R., Weitz, D.A., Martin, A.C., Park, J.-A., Butler, J.P., Fredberg, J.J., 2018. Nat. Phys. 14, 613.
Bailles, A., Collinet, C., Philippe, J.-M., Lenne, P.-F., Munro, E., Lecuit, T., 2019. Nature 572, 467.
Barriga, E.H., Mayor, R., 2019. Semin. Cell Dev. Biol. 93, 55.
Beysens, D.A., Forgacs, G., Glazier, J.A., 2000. Proc. Natl. Acad. Sci. U. S. A. 97, 9467.
Bi, D., Lopez, J.H., Schwarz, J.M., Manning, M.L., 2015. Nat. Phys. 11, 1074.
Bi, D., Yang, X., Marchetti, M.C., Manning, M.L., 2016. Phys. Rev. X 6, 021011.
Bonn, D., Denn, M.M., Berthier, L., Divoux, T., Manneville, S., 2017. Rev. Mod. Phys. 89, 035005.
Bosveld, F., Bonnet, I., Guirao, B., Tlili, S., Wang, Z., Petitalot, A., Marchand, R., Bardet, P.-L., Marcq, P., Graner, F., Bellaiche, Y., 2012. Science 336, 724.
C. Duclut J. Paijmans M. M. Inamdar C. Modes F. Jülicher, in preparation.
Chiang, M., Marenduzzo, D., 2016. EPL 116, 28009.
Comelles, J., Ss, S., Lu, L., Maout, E.Le, Anvitha, S., Salbreux, G., Jülicher, F., Inamdar, M.M., Riveline, D., 2021. elife 10, e57730.
Curran, S., Strandkvist, C., Bathmann, J., de Gennes, M., Kabla, A., Salbreux, G., Baum, B., 2017. Dev. Cell 43, 480.
Duclut, C., Sarkar, N., Prost, J., Jülicher, F., 2019. Proc. Natl. Acad. Sci. U. S. A. 116, 19264.

Duclut, C., Prost, J., Jülicher, F., 2021. Proc. Natl. Acad. Sci. U. S. A. 118, e2021972118.
Duda, M., Kirkland, N.J., Khalilgharibi, N., Tozluoglu, M., Yuen, A.C., Carpi, N., Bove, A., Piel, M., Charras, G., Baum, B., Mao, Y., 2019. Dev. Cell 48, 245.
Dye, N.A., Popović, M., Spannl, S., Etournay, R., Kainmüller, D., Ghosh, S., Myers, E.W., Jülicher, F., Eaton, S., 2017. Development 144, 4406.
Dye, N.A., Popovic, M., Iyer, K.V., Fuhrmann, J.F., Piscitello-Gómez, R., Eaton, S., Jülicher, F., 2021. eLife10, e57964. https://doi.org/10.7554/eLife.57964.
Etournay, R., Popović, M., Merkel, M., Nandi, A., Blasse, C., Aigouy, B., Brandl, H., Myers, G., Salbreux, G., Jülicher, F., Eaton, S., 2015. elife 4, e07090.
Farhadifar, R., Röper, J.-C., Aigouy, B., Eaton, S., Jülicher, F., 2007. Curr. Biol. 17, 2095.
Firmino, J., Rocancourt, D., Saadaoui, M., Moreau, C., Gros, J., 2016. Dev. Cell 36, 249.
Fletcher, A.G., Osterfield, M., Baker, R.E., Shvartsman, S.Y., 2014. Biophys. J. 106, 2291.
Forgacs, G., Foty, R.A., Shafrir, Y., Steinberg, M.S., 1998. Biophys. J. 74, 2227.
Garcia, S., Hannezo, E., Elgeti, J., Joanny, J.-F., Silberzan, P., Gov, N.S., 2015. Proc. Natl. Acad. Sci. U. S. A. 112, 15314.
Gho, M., Schweisguth, F., 1998. Nature 393, 178.
Grosser, S., Lippoldt, J., Oswald, L., Merkel, M., Sussman, D.M., Renner, F., Gottheil, P., Morawetz, E.W., Fuhs, T., Xie, X., Pawlizak, S., Fritsch, A.W., Wolf, B., Horn, L.-C., Briest, S., Aktas, B., Manning, M.L., Käs, J.A., 2021. Phys. Rev. X 11, 011033.
Guirao, B., Rigaud, S.U., Bosveld, F., Bailles, A., López-Gay, J., Ishihara, S., Sugimura, K., Graner, F., Bellaïche, Y., 2015. elife 4, e08519.
Heisenberg, C.-P., Bellaïche, Y., 2013. Cell 153, 948.
Honda, H., Yamanaka, H., Dan-Sohkawa, M., 1984. J. Theor. Biol. 106, 423.
Iyer, K.V., Piscitello-Gómez, R., Paijmans, J., Jülicher, F., Eaton, S., 2019. Curr. Biol. 29, 578.
Jain, A., Ulman, V., Mukherjee, A., Prakash, M., Cuenca, M.B., Pimpale, L.G., Münster, S., Haase, R., Panfilio, K.A., Jug, F., Grill, S.W., Tomancak, P., Pavlopoulos, A., 2020. Nat. Commun. 11, 5604.
Kim, S., Pochitaloff, M., Stooke-Vaughan, G.A., et al., 2021. Embryonic tissues as active foams. *Nat. Phys.* 17, 859–866. https://doi.org/10.1038/s41567-021-01215-1.
Krajnc, M., Dasgupta, S., Ziherl, P., Prost, J., 2018. Phys. Rev. E 98, 022409.
Lees, A.W., Edwards, S.F., 1972. J. Phys. C Solid State Phys. 5, 1921.
Marchetti, M.C., Joanny, J.F., Ramaswamy, S., Liverpool, T.B., Prost, J., Rao, M., Simha, R.A., 2013. Rev. Mod. Phys. 85, 1143.
Marmottant, P., Mgharbel, A., Kafer, J., Audren, B., Rieu, J.-P., Vial, J.-C., van der Sanden, B., Maree, A.F.M., Graner, F., Delanoe-Ayari, H., 2009. Proc. Natl. Acad. Sci. U. S. A. 106, 17271.
Matoz-Fernandez, D.A., Agoritsas, E., Barrat, J.-L., Bertin, E., Martens, K., 2017. Phys. Rev. Lett. 118, 158105.
Merkel, M., 2014. From Cells to Tissues: Remodeling and Polarity Reorientation in Epithelial Tissues. TU Dresden.
Merkel, M., Etournay, R., Popović, M., Salbreux, G., Eaton, S., Jülicher, F., 2017. Phys. Rev. E 95, 032401.
Mitchel, J.A., Das, A., O'Sullivan, M.J., Stancil, I.T., DeCamp, S.J., Koehler, S., Ocaña, O. H., Butler, J.P., Fredberg, J.J., Nieto, M.A., Bi, D., Park, J.-A., 2020. Nat. Commun. 11, 5053.
Molnar, K., Labouesse, M., 2021. Open Biol. 11, 210006.
Mongera, A., Rowghanian, P., Gustafson, H.J., Shelton, E., Kealhofer, D.A., Carn, E.K., Serwane, F., Lucio, A.A., Giammona, J., Campàs, O., 2018. Nature 561, 401.
Petridou, N.I., Heisenberg, C.-P., 2019. EMBO J. 38, e102497.
Petridou, N.I., Grigolon, S., Salbreux, G., Hannezo, E., Heisenberg, C.-P., 2019. Nat. Cell Biol. 21, 169.
Popović, M., Nandi, A., Merkel, M., Etournay, R., Eaton, S., Jülicher, F., Salbreux, G., 2017. New J. Phys. 19, 033006.
Popović, M., de Geus, T.W.J., Ji, W., Wyart, M., 2020. arXiv:2009.04963.
Popović, M., Druelle, V., Dye, N.A., Jülicher, F., Wyart, M., 2021. New J. Phys. 23, 033004.
Prost, J., Jülicher, F., Joanny, J.-F., 2015. Nat. Phys. 11, 111.
Ranft, J., Basan, M., Elgeti, J., Joanny, J.-F., Prost, J., Jülicher, F., 2010. Proc. Natl. Acad. Sci. U. S. A. 107, 20863.
Rauzi, M., Lenne, P.-F., Lecuit, T., 2010. Nature 468, 1110.
Saadaoui, M., Rocancourt, D., Roussel, J., Corson, F., Gros, J., 2020. Science 367, 453.
Sagner, A., Merkel, M., Aigouy, B., Gaebel, J., Brankatschk, M., Jülicher, F., Eaton, S., 2012. Curr. Biol. 22, 1296.
Sanematsu, P.C., Erdemci-Tandogan, G., Patel, H., Retzlaff, E.M., Amack, J.D., Manning, M.L., 2021. 3D viscoelastic drag forces drive changes to cell shapes during organogenesis in the zebrafish embryo. Cells & Development. https://doi.org/10.1016/j.cdev.2021.203718.
Sarkar, N., Prost, J., Jülicher, F., 2019. New J. Phys. 21, 043035.
Steffe, J.F., 1996. Rheological Methods in Food Process Engineering, 2nd ed. Freeman Press, East Lansing, Michigan.
Sussman, D.M., Paoluzzi, M., Cristina Marchetti, M., Lisa Manning, M., 2018. EPL 121, 36001.
Tetley, R.J., Staddon, M.F., Heller, D., Hoppe, A., Banerjee, S., Mao, Y., 2019. Nat. Phys. 15, 1195.
Tlili, S., Durande, M., Gay, C., Ladoux, B., Graner, F., Delanoë-Ayari, H., 2020. Phys. Rev. Lett. 125, 088102.
Vuong-Brender, T.T.K., Amar, M.Ben, Pontabry, J., Labouesse, M., 2017. elife 6, e23866.
Wang, Y., Nathans, J., 2007. Development 134, 647.
Wang, X., Merkel, M., Sutter, L.B., Erdemci-Tandogan, G., Manning, M.L., Kasza, K.E., 2020. Proc. Natl. Acad. Sci. U. S. A. 117, 13541.
Yamamoto, T., Sussman, D.M., Shibata, T., Manning, M.L., 2020. arXiv:2008.13007 (arXiv:2008.13007).